ACS APPLIED MATERIALS & INTERFACES

www.acsami.org
Research Article

Ultrasound Visualization of Spatiotemporal Autophagy-Regulated Nanodroplets for Amplifying ICB in Melanoma via Remodeling Tumor Inflammatory Microenvironment

Nianhong Wu, Qin Zhang, Rui Tang, Liming Deng, Yuting Cao, Benxin Fu, Hongmei Dong, Zeyan Huang, Li Wan, Hongye He, Yi Lin, Junjie Liu, Chunyu Xia,* and Pan Li*

Cite This: ACS Appl. Mater. Interfaces 2025, 17, 29364−29378

Read Online

ACCESS | Metrics & More | Article Recommendations | Supporting Information

ABSTRACT: Immune checkpoint blockade (ICB) therapy, represented by anti-PD-1/PD-L1 antibodies, is confronted with difficulties of unsatisfied response rates owing to the prevalence of "cold" immune tumor microenvironment (TME) in most cancers. Blocking cytoprotective autophagy has emerged as a potential strategy to remodel the inflammatory TME. Nevertheless, the dual roles of autophagy in tumor progression, coupled with the poor pharmacokinetic properties of small-molecule autophagy inhibitors, significantly restrict clinical applications. To address these challenges, a low-intensity focused ultrasound (LIFU) responsive phase-change nanodroplet delivery platform (SP@Lip-PEG) is elaborately developed to deliver specific autophagy inhibitor SAR405 for activating typical tumor-resident immune cells. The PEG-modified nanodroplets effectively accumulate into the tumor site. Upon LIFU activation, SP@Lip-PEG transforms into microbubbles through acoustic droplet vaporization (ADV) effects, enabling the controlled release of SAR405 under ultrasound imaging guidance. The released SAR405 significantly triggered the upregulation of proinflammatory factors CCL5 and CXCL10 through autophagy manipulation, creating an inflammatory TME to facilitate the recruitment of natural killer (NK) cells and $CD8^+$ T cells, along with promoting dendritic cell (DC) maturation and synergistically enhancing ICB efficacy. With the high specificity of SAR405 and the controllable therapeutic process under LIFU irradiation, this noninvasive, efficient, and cost-effective drug delivery vector opened new horizons for conquering the clinical dilemma of rescuing ICB response rates.

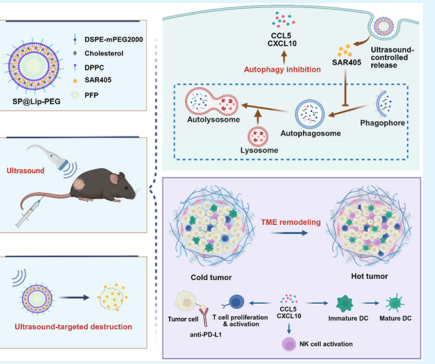

KEYWORDS: *ultrasound-targeted drug release, autophagy inhibition, immune checkpoint blockade therapy, low-intensity focused ultrasound, phase-change nanodroplet*

1. INTRODUCTION

Immune checkpoint blocking (ICB) therapy is typically represented by PD-1/PD-L1 blocking, which could reinvigorate T cell functions by impeding the binding of PD-L1 on cancer cells to PD-1 on T cells, greatly revolutionizing cancer immunotherapy.[1,2] However, as a monotherapy, only 20−40% of melanoma patients treated with anti-PD-1/PD-L1 antibodies exhibit ideal clinical benefits, indicating obvious limitations and the need for significant improvement in the current ICB treatment mode.[3] The response rates of ICB critically depend on the interactions between tumor cells and tumor immune microenvironment.[4] Most patients exhibit intrinsic drug resistance due to defects in tumor antigen presentation or poor $CD8^+$ T cell infiltration caused by insufficient chemokines secretion in the tumor microenvironment (TME), known as the "cold tumor".[5,6] It has been demonstrated that the combination of SDT and αPD-L1 effectively inhibited the progression of melanoma by promoting the infiltration of cytotoxic T lymphocytes.[7] Therefore, seeking potential and potent strategies to boost the immune responses in TME to promote T cell infiltration and transform "immune-cold" into "immune-hot" tumors has emerged as a crucial method to improve the current restricted ICB efficiency.

Various combination strategies have been explored to enhance the efficiency of ICB therapy; the results were not particularly satisfactory for researchers until now. For example, therapeutic cancer vaccines have made great progress in combination with anti-PD-L1 antibodies.[8] However, the therapeutic efficacy was much less consistent than expected owing to the tumor immunosuppressive microenvironment, the instability, and the nonspecific distribution of vaccine formulations *in vivo*.[9] STING agonists could help to facilitate the antitumor immunotherapy through inducing type I

Received: February 20, 2025
Revised: April 27, 2025
Accepted: April 30, 2025
Published: May 7, 2025

https://doi.org/10.1021/acsami.5c03394
ACS Appl. Mater. Interfaces 2025, 17, 29364−29378

Scheme 1. Illustration of LIFU-Responsive SP@Lip-PEG for Improving ICB Therapy by Inhibiting Autophagy to Secret Proinflammatory Factors to Shape the Inflammatory TME. Created with BioRender

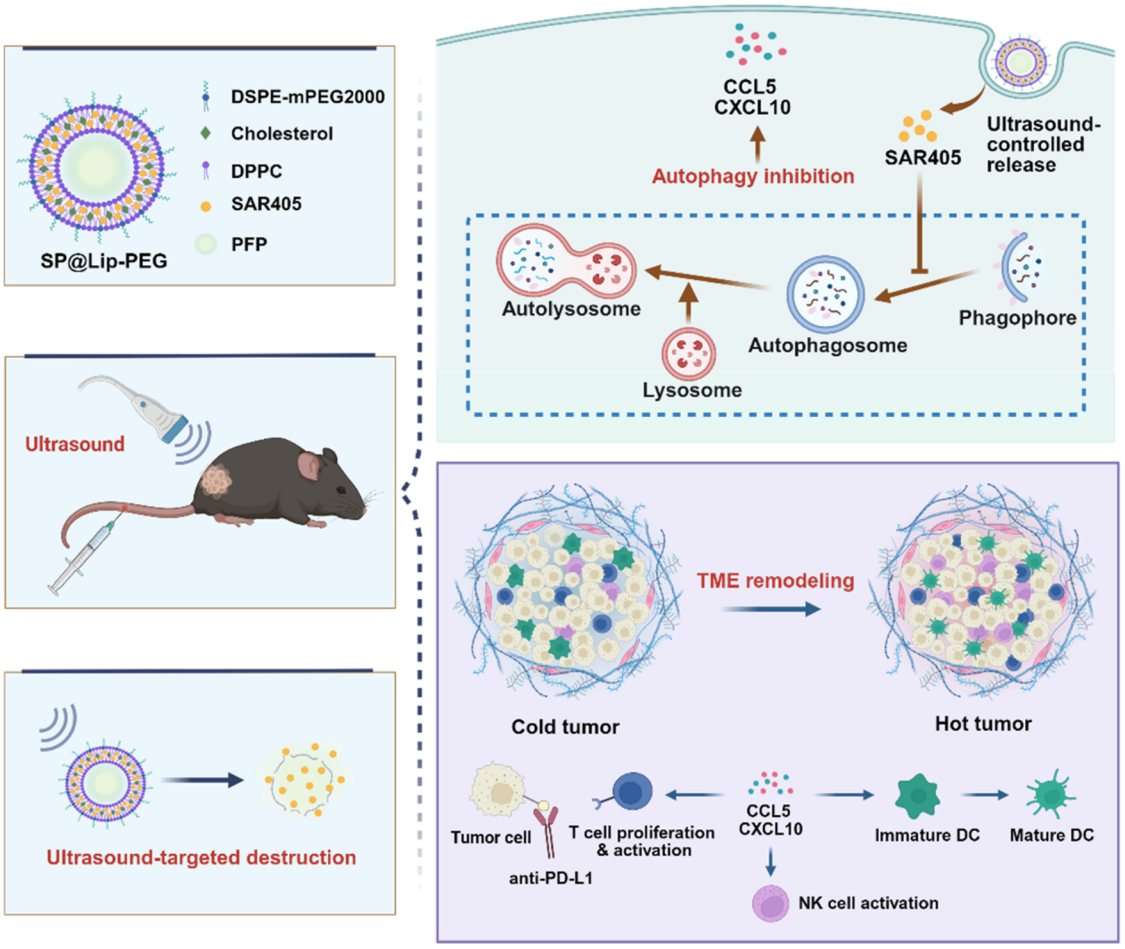

interferon release to promote immune cell recruitment,[10] while sustained hyperactivation of the cGAS-STING pathway may drive paradoxical immunosuppressive effects in certain tumor contexts and lead to severe inflammatory storms.[6,11,12] Although the combination of ICB with chemotherapy, radiotherapy, and photodynamic therapy exhibited specific effects to improve anticancer therapy, none of the related drugs have come to the clinical stage, suggesting the existing restrictions of the currently developed formulations. Therefore, developing a new-type nanoformulation that possesses a favorable ability to reprogram cold TME and promote immune cell infiltration, along with good safety and clinical translational potential, represents a vital strategy to optimize the current antitumor ICB therapy efficiency.

These days, strategies like enhancing tumor immunogenicity through inflammatory regulation to remodel "cold" TME exhibit good potential to synergize ICB.[13] Notably, autophagy, an important physiological process for cellular homeostasis maintenance, is also deeply involved in the networks of tumor inflammation, immune activation, and amplifying ICB therapy.[14,15] Yamamoto et al. revealed that the inhibition of autophagy could restore the MHC-I level, resulting in stronger antigen presentation and activating downstream antitumor T cell responses.[16] As expected, the combination of autophagy inhibition with dual ICBs (anti-PD-1 and anti-CTLA-4) enhanced the antitumor immune responses in this study. Therefore, searching for an efficient autophagy inhibition strategy represents a potential method to remodel a cold TME via autophagy manipulation for synergizing ICB.

SAR405, a typical Vps34 kinase-selective autophagy inhibitor, possesses the inherent capacity to suppress the autophagy activity of tumor cells.[17] Notably, Noman et al. have reported that the treatment of SAR405 could promote the release of the proinflammatory factors CCL5 and CXCL10.[13] And autophagy inhibition also enhanced the efficiency of ICB by facilitating the infiltration of natural killer (NK) cells and cytotoxic T lymphocytes (CTLs) through elevating the inflammation of TME.[13] Thus, SAR405 emerged as a good small-molecule agent to shape the inflammatory TME through autophagy manipulation for synergizing ICB. However, the further clinical application of many small-molecule inhibitors (such as SAR405) is generally impeded by various challenges. For example, SAR405 encounters issues related to poor hydrophilicity, low stability, and limited bioavailability, necessitating frequent administration and large doses over extended periods to provide long-acting therapy.[18,19] In addition, the nonspecific distribution of SAR405 could also produce toxic side effects, such as impairing long-term memory.[20] Therefore, it is crucial to develop a safe and efficient delivery system to release SAR405 on demand in the tumor region while reducing the toxicities to surrounding tissues and cells.

Ultrasound-mediated drug-controlled-release systems have been confirmed by many research studies to enhance drug

https://doi.org/10.1021/acsami.5c03394
ACS Appl. Mater. Interfaces 2025, 17, 29364−29378

permeability and delivery accuracy, along with reducing unfavorable side effects during cancer treatment.[21,22] Nanodroplets represent one of the typical sono-responsive phase-change nanomaterials, possessing obvious superiorities of tumor accumulation capacity, systemic circulation stability, and acoustic droplet vaporization (ADV)-elicited drug-responsive release ability.[23] Moreover, the triggering mode of the physically responsive drug-controlled-release systems is simple. The ability to trigger drug release with spatiotemporal specificity using a physically ultrasound-stimulated manner is of great irreplaceable advantages compared to the release manner based on the exogenous stimuli to TME.[24] Thus, the ultrasound-activated phospholipid-based nanodroplets emerge as an ideal nanocarrier for realizing the targeted delivery of SAR405 into tumor regions. On the one hand, a higher concentration of drug accumulation might be realized in the target tumor area owing to the explosion of the drug-loaded nanodroplets under the ultrasound-targeted destruction (UTD) effects, thereby enhancing the therapeutic effects and lowering the systemic toxicities.[25,26] On the other hand, ultrasound irradiation might elicit obvious acoustic cavitation effects, with bubbles oscillating, contracting, and collapsing to form jets, shock waves in the surroundings, and acoustic pores in the vascular walls or cell membranes.[27] Consequently, local vascular permeability and cell membrane permeability could be further enhanced to boost drug penetration and cellular internalization.[23] It is also worth noting that just because autophagy usually plays perplexing double-edged sword roles in antitumor therapy, it is a good opportunity to directly reveal the intrinsic regulatory effects of the SAR405-mediated autophagy inhibition on tumor inflammation and immunity through the fabricated SAR405-loaded nanodroplet nanosystem.

Given this, we proposed to prepare a PEG-modified fluorocarbon phase-change nanodroplet loaded with autophagy inhibitor SAR405 to achieve targeted and controlled release of SAR405 for enhancing cellular autophagy inhibition and also synergizing ICB. As shown in Scheme 1, the PEG-modified nontoxic phospholipid-based nanodroplets improved biocompatibility and prolonged blood circulation time. Simultaneously, the nanoplatform with a minimal liquid core efficiently carried SAR405 and effortlessly navigated through the tumor vascular endothelial gap to aggregate into the tumor site. Upon exposure to low-intensity focused ultrasound (LIFU), it responsively transformed into gas-cored microbubbles. When the microbubbles were disrupted, the cavitation effects could enhance the permeability of tumor cells, allowing SAR405 to be effectively internalized by cells and act in the cells, thereby improving the impacts on autophagy inhibition. After autophagy blockade, tumor cells released proinflammatory factors, including CCL5 and CXCL10, which could elevate the inflammation level in the TME. The release of CCL5 and CXCL10 further promoted the recruitment of functional NK cells and CTLs into the TME, along with promoting DC maturation, thus potentiating the therapeutic efficacy of anti-PD-L1 antibody and reducing the tumor burden. Therefore, with the superiorities of the lipid material-based nanodroplets as one of the most potential nanodrugs for clinical translation and the accessibility of ultrasound in the clinic, a noninvasive, efficient, and simple drug delivery system with an autophagy inhibitor-based ICB effective sensitization strategy was innovatively reported in this research.

2. MATERIALS AND METHODS

2.1. Materials. 1,2-Dipalmitoyl-*sn*-glycero-3-phosphocholine (DPPC) and 1,2-distearoyl-*sn*-glycero-3-phosphoethanolamine-*N*-[methoxy(polyethylene glycol)-2000] (DSPE-mPEG2000) were purchased from Xi'an Ruixi Biological Technology Co., Ltd. (Xi'an, China). Cholesterol was purchased from Sangon Biotech (Shanghai, China). Perfluoropentane (PFP) was ordered from Strem Chemicals (MA). SAR405 was purchased from MCE (Shanghai, China). Anti-mouse PD-L1 (B7−H1) was acquired from Bioxcell (Lebanon). ELISA kits were acquired from Jiubang Biotech Co. Ltd. (Quanzhou, China). The following antibodies of BioLegend were used: FITC anti-mouse CD3 (100204), PerCP/Cyanine 5.5 anti-mouse NK-1.1 (108727), PE anti-mouse CD4 (100408), APC anti-mouse CD8a (100712), FITC anti-mouse CD11c (117306), PE anti-mouse CD80 (104708), and APC anti-mouse CD86 (105012). Mouse CCL5/RANTES antibody was purchased from R&D Systems (MAB478).

2.2. Cell Lines and Animal Model. B16−F10 cells, provided by Chongqing Medical University, were cultured in RPMI 1640 medium (Gibco) with 10% fetal bovine serum (Biological Industries) and 1% penicillin/streptomycin (Gibco) as dietary supplements at 37 °C and 5% CO_2. Female C57BL/6J mice, 6 to 8 weeks old, were bought from the Chongqing Medical University Animal Center. The *in vivo* experimental protocols were approved by the Ethics Committee of the Second Affiliated Hospital of Chongqing Medical University. B16−F10 cells in the logarithmic growth phase were resuspended to a concentration of 2×10^6 cells mL^{-1} with PBS. Mice were injected with 100 μL of B16−F10 cell suspensions in the right flank to establish a subcutaneous melanoma tumor model.

2.3. Synthesis of SP@Lip-PEG. According to the filming-rehydration method and the acoustic vibration method established by previous reports, the nanodroplet encapsulating SAR405 was synthesized. First, DPPC (6 mg), DSPE-mPEG2000 (2 mg), cholesterol (2 mg), and SAR405 (500 μg) were dissolved in 10 mL of trichloromethane and methyl alcohol with an ultrasonic cleaner for 2 min. A uniformly dried lipid film was generated in a rotary evaporator (30 min at 50 °C and 100 rpm). Next, a mixture was obtained by adding 200 μL of PFP to the lipid film solution hydrated with 4 mL of PBS. Finally, SP@Lip-PEG was produced by shaking the mixture under ultrasonication in ice bath conditions and centrifugation at 8000 rpm for 5 min.

2.4. Characterization of SP@Lip-PEG. The dispersion of SP@Lip-PEG was observed by confocal laser scanning microscopy (CLSM) (Nikon, A1, Japan), and the morphology of SP@Lip-PEG was observed under transmission electron microscopy (TEM) (Hitachi H-7600, Japan). NanoBrook Omni instrument (Brookhaven, U.K.) was applied to investigate the particle size and ζ-potential of SP@Lip-PEG. The ultraviolet−visible (UV−vis) spectrum of SAR405 in SP@Lip-PEG was detected by a UV-3600 spectrophotometer (Shimazu, Japan). Then, the standard curve of SAR405 was examined, and the SAR405 concentration in SP@Lip-PEG was calculated via UV−vis spectrometry as follows: SAR405 encapsulation efficiency (E.E.) (%) = mass of SAR405 encapsulated/total mass of SAR405 × 100%. SAR405 loading efficiency (%) = mass of SAR405 encapsulated/total mass of nanodroplets × 100%.

2.5. *In Vitro* LIFU-Responsive Release of SAR405 from SP@Lip-PEG under Ultrasound Imaging Monitoring. To evaluate the *in vitro* ultrasound imaging capability of SP@Lip-PEG and determine the optimal irradiation parameters, we utilized a 3% agar (w/v) gel model for testing. First, SP@Lip-PEG (250 μg mL^{-1}) was treated with different LIFU irradiation powers (0, 1.0, 2.0, 3.0, and 4.0 W cm^{-2}) and irradiation times (0, 1, 2, 3, and 4 min). Subsequently, B-mode and contrast-enhanced ultrasound (CEUS) mode (Visual Sonics Inc., Toronto, Canada) was used to assess the imaging performance of SP@Lip-PEG in gel wells.

The drug release profile of the LIFU-responsive SP@Lip-PEG was characterized in two groups (SP@Lip-PEG with and without LIFU) using a dialysis method. Briefly, dialysis bags (3500 Da MWCO) containing SP@Lip-PEG solution were placed in a flask of 35 mL of slow-release medium (containing 0.1% Tween-80, 30% anhydrous

https://doi.org/10.1021/acsami.5c03394
ACS Appl. Mater. Interfaces 2025, 17, 29364−29378

ethanol, and 0.02% sodium azide) and slowly shaken. Then, one of the bags containing SP@Lip-PEG was exposed to ultrasonic irradiation (3 W cm^{-2}, 3 min), and ultrasound was applied at 4 h intervals for 3 exposures. At predetermined times (0, 1, 2, 4, 5, 6, 8, 9, 10, 12, 13, 14, 16, 20, and 24 h), 1 mL of buffer was collected for detection, and 1 mL of fresh buffer was readded into the container. Finally, the UV absorbance was detected for calculating the cumulative release rate of SAR405.

2.6. *In Vivo* Ultrasound Imaging Activity and Drug Release Properties of SP@Lip-PEG. To determine the optimal time point for irradiation with LIFU *in vivo*, DiD-labeled SP@Lip-PEG (1.0 mg mL^{-1}) was intravenously injected into subcutaneous melanoma-bearing mice (n = 3). Then, fluorescence imaging (FLI) was captured using the IVIS imaging system at specific time points (0, 1, 4, 8, 24, and 48 h).

For *in vivo* ultrasound imaging, SP@Lip-PEG (1.0 mg mL^{-1}, 200 μL) was intravenously injected into B16−F10 tumor-bearing mice (n = 3). A VisualSonics system with the LZ-250 sensor was applied to record B-mode and CEUS images at specified periods, including before treatment (pre), 8 h after injection (8 h), and 8 h after injection with LIFU (8 h + LIFU). The ultrasound imaging was performed using the following parameters: frequency of 18 MHz, power set at 4%, contrast gain adjusted to 35.0 dB, and two-dimensional (2D) gain set to 18.0 dB. The ultrasonic parameters were 1.0 MHz, 3 W cm^{-2}, and a 50% duty cycle with a 5 min sonication duration. The signal intensities of the B-mode and CEUS mode were measured using an ultrasonic image analyzer (DFY-II, Institute of Ultrasonic Imaging, Chongqing Medical University).

B16−F10 Tumor-bearing mice were randomly divided into two groups: (1) 8 h and (2) 8 h + LIFU. Next, SP@Lip-PEG was injected into the tail vein of mice, and one group was irradiated with LIFU after 8 h (parameters as above). After 1 h, tumor tissues from both groups were collected and weighed. The samples were then treated with extract solvent (acetonitrile/methanol/water = 2:2:1, precooled at −20 °C) and vortexed. After homogenization, the supernatant was collected and centrifuged at 12000 rpm for 15 min for UHPLC-MRM-MS/MS analysis.

2.7. Cellular Uptake and Cytotoxicity Assay. DiI-labeled SP@Lip-PEG was incubated with melanoma cells cultured in confocal dishes for 1, 2, and 4 h, respectively. After the cells were washed with PBS, 4% paraformaldehyde (500 μL) was used for fixation at room temperature for 15 min. Subsequently, the nuclei were stained with DAPI (200 μL) for 10 min. And CLSM was used to detect the intracellular distribution of SP@Lip-PEG. Similarly, the intracellular uptake of SP@Lip-PEG at different time points was quantitatively analyzed *via* flow cytometry.

The CCK-8 assay assessed the cytotoxicity of SP@Lip-PEG with LIFU irradiation (3 W cm^{-2}, 3 min). Concretely, B16−F10 cells (2×10^4) were seeded and incubated overnight in 96-well plates. Subsequently, cell viability was determined by a CCK-8 assay after incubation with different concentrations of SP@Lip-PEG (0, 25, 50, 75, 100, and 125 μg mL^{-1}) for 24 h. In addition, B16−F10 cells were set as follows: (1) P@Lip-PEG (no SAR405 and LIFU), (2) P@Lip-PEG (no LIFU), (3) SP@Lip-PEG (no LIFU), and (4) SP@Lip-PEG + LIFU. The concentration of nanoparticles was 125 μg mL^{-1}. The cytotoxicity of different treatments on B16−F10 cells was analyzed by the CCK-8 assay.

B16−F10 cells seeded in 6-well plates were divided into the following 6 groups: (1) Control (no treatment), (2) LIFU, (3) P@Lip-PEG (no SAR405 and LIFU), (4) P@Lip-PEG + LIFU (no SAR405), (5) SP@Lip-PEG (no LIFU), and (6) SP@Lip-PEG + LIFU. The concentration of nanoparticles and the parameters of LIFU irradiation were the same as above. Cell viability was determined by calcein-AM/PI staining under CLSM, coupled with the Annexin V-FITC/PI method, to analyze the proportion of apoptosis in each group.

2.8. Intracellular Level of Autophagy Determined by Western Blot. To investigate the effect of SR405 on the intracellular level of autophagy, we incubated B16−F10 tumor cells with P@Lip-PEG, SP@Lip-PEG, or free SAR405 with an equivalent concentration (approximately 4 μg mL^{-1}) for 24 h under predetermined conditions. The drug in the nanoparticles was released by LIFU irradiation. Next, cells were lysed in lysis buffer (RIPA lysis buffer/phosphatase inhibitor/protease inhibitor = 100:10:1) for 30 min. The proteins were obtained by centrifuging the cell lysates at 12000 rpm for 15 min at 4 °C. Equal amounts of proteins were separated by 12.5% SDS-polyacrylamide gel electrophoresis (Epizyme Biotech). Following the transfer of proteins onto a 0.22 μm PVDF membrane, they were blocked for 2 h at room temperature with 5% skim milk. They were then incubated overnight at 4 °C with the primary antibody (anti-IRF7 antibody, Proteintech group; anti-STAT1 antibody, Proteintech group; anti-LC3B antibody, Proteintech group; anti-p62 antibody, ABclonal Technology Co Ltd.; β-actin antibody, Boster). After the membrane was washed with TBST buffer, it was incubated with the appropriate secondary antibodies for 1 h at room temperature. Finally, protein signals were displayed with a chemiluminescence system (Bio-Rad).

2.9. Antitumor Efficacy *In Vivo*. Seven days after the injection of tumor cells, B16−F10 tumor-bearing mice were randomly divided into five groups (n = 5): (1) Control, (2) P@Lip-PEG + LIFU, (3) SP@Lip-PEG, (4) SAR405, and (5) SP@Lip-PEG + LIFU. On days 8, 9, and 10, respectively, mice were administered 200 μL of PBS, P@Lip-PEG (1.0 mg mL^{-1}), SAR405 (200 μg mL^{-1}), or SP@Lip-PEG (1.0 mg mL^{-1}) *via* the tail vein. Eight hours after injection, the tumor site was irradiated with ultrasound (50% duty cycle, 1.0 MHz, 3 W cm^{-2}) for 5 min. During the treatment, the ultrasound probe was moved around the tumor so that the entire tumor was wholly covered. Tumor volume and body weight were monitored every 2 days, and the volume was calculated as follows: Volume = (Length/$Width^2$)/2 mm^3. When the tumor volume reached 1000 mm^3, the mice were euthanized by cervical dislocation. The tumor was excised and preserved with 4% paraformaldehyde. The tumors underwent H&E, terminal deoxynucleotidyl transferase dUTP nick end labeling (TUNEL), and Ki67 immunofluorescence staining to confirm the treatment efficiency.

2.10. Immune Response *In Vivo*. Tumor-bearing mice were divided into groups and treated as described above to investigate the immunoregulatory effects of various formulations *in vivo*. The harvested tumors and draining lymph nodes were mechanically dissected into fragments. Subsequently, single-cell suspensions were prepared by an enzymatic hydrolysis method, and red blood cells were lysed with red blood cell lysate (Biosharp). After being washed with PBS, cells were stained with the corresponding fluorescently labeled antibodies according to the protocols recommended by the manufacturers. In concrete terms, DC cells were labeled with FITC anti-mouse CD11c, PE anti-mouse CD80, and APC anti-mouse CD86. NK cells were detected with FITC anti-mouse CD3 and PerCP/Cyanine 5.5 anti-mouse NK-1.1. FITC anti-mouse CD3, PE anti-mouse CD4, and APC anti-mouse CD8a were used to mark T lymphocytes. Finally, we performed single-dye staining as a compensating control and analyzed the prepared cell suspensions by flow cytometry. At the same time, we also conducted *in vivo* chemokine depletion tests. First, CCL5 blockade was achieved through intravenous injection of the Mouse CCL5/RANTES Antibody (2.5 mg kg^{-1}) 24 h prior to tumor cell implantation and first treatment. Next, unilateral B16−F10 tumor-bearing mice were randomized into 2 groups: SP@Lip-PEG + LIFU + α-CCL5 and SP@Lip-PEG + LIFU. The protocol of SP@Lip-PEG and LIFU is the same as above. For the SP@Lip-PEG + LIFU + α-CCL5 group, CCL5 neutralizing antibody was administered twice weekly to maintain continuous chemokine blockade until the end of the experiment. During the treatment, tumor volume and mice body weight were monitored every 2 days.

2.11. *In Vivo* Efficacy of Combining SP@Lip-PEG and ICB Treatment. To assess the anticancer effect of combined autophagy inhibition and ICB therapy *in vivo*, 20 tumor-bearing mice (7 days after tumor cell inoculation) were randomly assigned to 4 groups (n = 5): (1) Control, (2) PD-L1, (3) SP@Lip-PEG + LIFU, and (4) SP@Lip-PEG + LIFU + PD-L1. On days 8, 9, and 10, 200 μL of SP@Lip-PEG (1.0 mg mL^{-1}) was injected intravenously, and ultrasound

https://doi.org/10.1021/acsami.5c03394
ACS Appl. Mater. Interfaces 2025, 17, 29364−29378

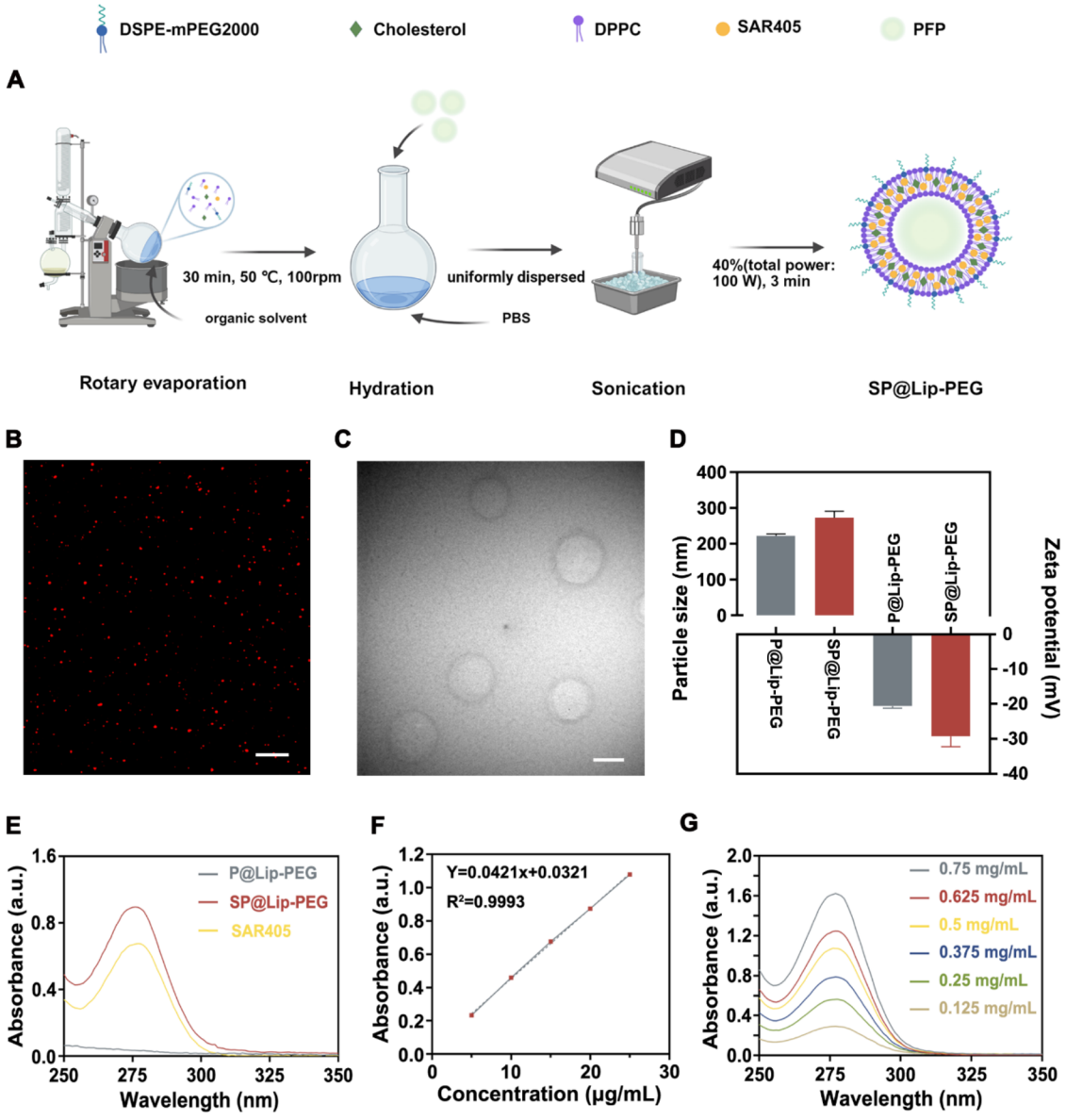

Figure 1. Preparation and Characterization of SP@Lip-PEG. (A) Preparation process of SP@Lip-PEG. Created with BioRender. (B) CLSM image of DiI-labeled SP@Lip-PEG (Scale bar: 20 μm). (C) The TEM image of SP@Lip-PEG (Scale bar: 100 nm). (D) The hydrodynamic diameter and ζ-potential of SP@Lip-PEG (n = 3). (E) UV absorption spectra of SAR405, P@Lip-PEG, and SP@Lip-PEG. (F) Standard curve of SAR405 at 277 nm. (G) UV absorption spectra of SP@Lip-PEG with different concentrations. Data are represented as mean ± SD.

irradiation was conducted 8 h later (parameters are the same as the method above). Additionally, for the PD-L1-related group, anti-PD-L1 antibodies (1.5 mg kg^{-1}) were administered intravenously on days 9, 11, and 13. The body weight and tumor volume of the mice were monitored during treatment. The removed tumors were made into single-cell suspensions, and the phenotypes of NK cells and T lymphocytes were analyzed by flow cytometry to verify the regulation efficiency of various treatments on the immune cell infiltration in the tumor.

2.12. Statistical Analysis. Data for statistical analysis were expressed as means ± standard deviations. One-way analysis of variance (ANOVA), followed by Tukey correction, was used to make multiple comparisons. Student's two-tailed t-test examined the two groups and analysis. $P < 0.05$ was considered statistically significant.

3. RESULTS AND DISCUSSION

3.1. Synthesis and Characterization of SP@Lip-PEG. As shown in Figure 1A, SP@Lip-PEG was synthesized *via* traditional thin-film hydration and sonication methods. In this study, DSPE was modified with PEG to enhance *in vivo* circulation longevity. Subsequently, the hydrophobic molecule PFP was then entrapped within the core, while the lipophilic drug SAR405 was integrated into the phospholipid bilayer. CLSM revealed that DiI-labeled SP@Lip-PEG was homogeneously dispersed in PBS (Figure 1B). The TEM image in Figure 1C further confirmed that SP@Lip-PEG was spherical and uniformly nanosized. Compared with P@Lip-PEG, the hydrodynamic diameter of SP@Lip-PEG increased from 222.95 ± 5.18 to 273.24 ± 17.96 nm with a polydispersity index (PDI) of 0.15 ± 0.09, and the ζ-potential varies from −20.59 ± 0.61 to −29.30 ± 2.96 mV (Figures S1, S2, and 1D). Furthermore, the average hydrodynamic diameter of SP@Lip-PEG remained stable in 10% fetal bovine serum (FBS) and PBS buffer for 5 days, indicating its excellent colloidal stability in the physiological environment (Figure S3). Under the UV

https://doi.org/10.1021/acsami.5c03394
ACS Appl. Mater. Interfaces 2025, 17, 29364−29378

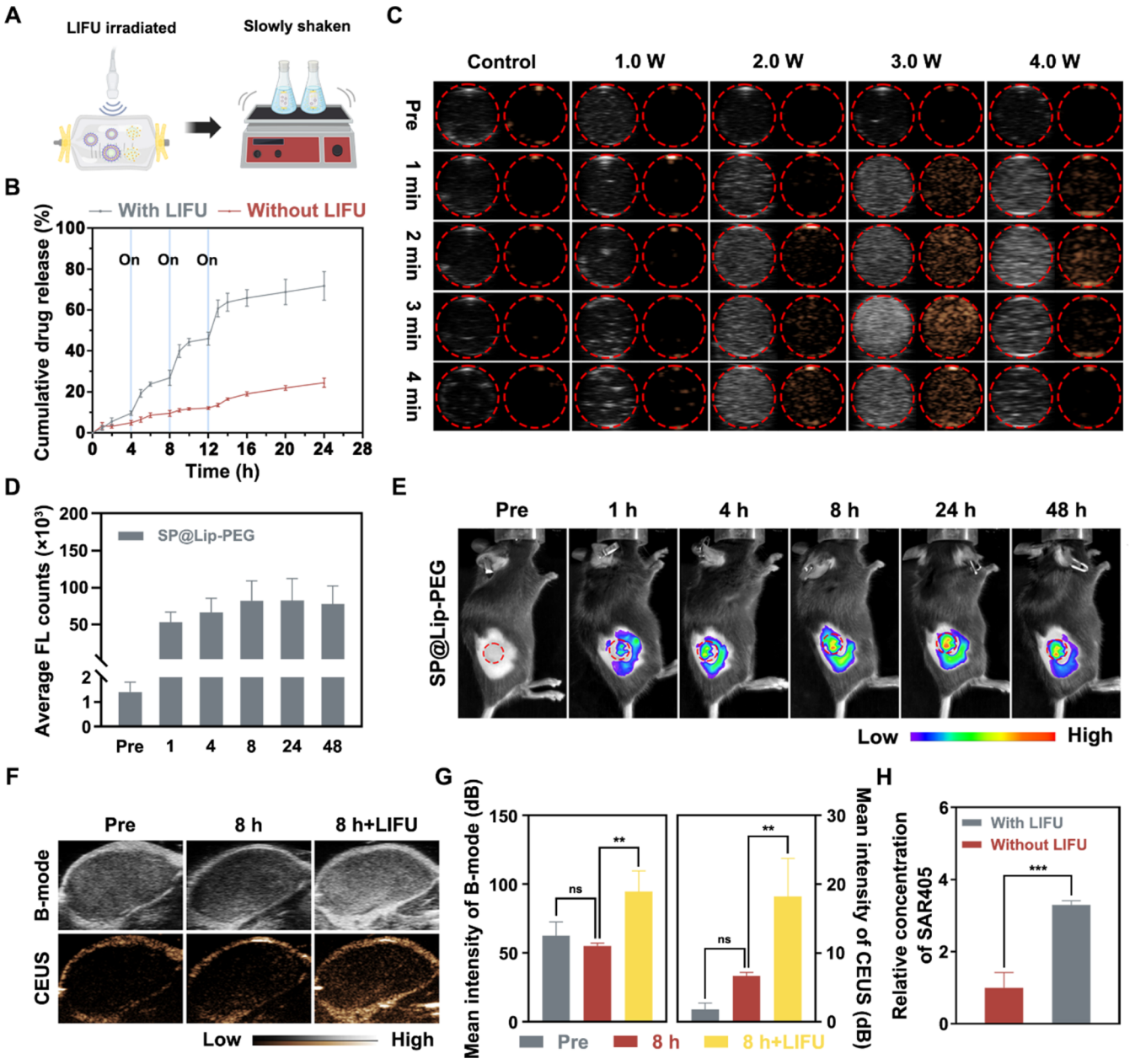

Figure 2. LIFU-responsive release of SAR405 from SP@Lip-PEG under ultrasound imaging monitoring. (A) Schematic illustration of LIFU-responsive drug release. Created with BioRender. (B) The SAR405 cumulative release from SP@Lip-PEG with or without 3 episodes of LIFU activation over 24 h. (C) The B-mode/CEUS-mode imaging of SP@Lip-PEG after LIFU irradiation with different power intensities or irradiation times. (E) *In vivo* FLI of B16−F10 tumor-bearing mice after intravenous injection of SP@Lip-PEG and (D) relative time-dependent FLI signal intensity. (F) The B-mode/CEUS-mode imaging and corresponding mean intensity (G) of B16−F10 tumor-bearing mice under different conditions. (H) Quantitative analysis of SAR405 in tumors treated with or without LIFU at 8 h. Data are represented as the mean ± SD (n = 3). *p < 0.05, **p < 0.01, ***p < 0.001.

spectra of SP@Lip-PEG (Figure 1E), the characteristic absorption peak of SAR405 was intuitively displayed at 277 nm, confirming the successful encapsulation of SAR405 within the nanodroplets. The UV technique was then used to establish the standard curve of SAR405, and the resulting linear regression equation was $Y = 0.0421X + 0.0321$, with $R^2 = 0.999$ (Figure 1F). With the increase in drug dosage, the entrapment efficiency decreased, and the drug loading increased. Apparently, the maximum benefit was achieved with a 500 μg dosage, resulting in an E.E. of 87.54 ± 1.84% and a drug loading of 4.17 ± 0.09% (Figures S4 and 1G). In summary, we successfully synthesized a phase-change nanodroplet (SP@Lip-PEG) loading with SAR405.

3.2. LIFU-Responsive Release of SAR405 from SP@Lip-PEG under Ultrasound Imaging Monitoring. The initial step to verify the LIFU-controlled drug release from SP@Lip-PEG was to confirm the potential for phase transition and to inspect whether LIFU could serve as a driving force for this process. SP@Lip-PEG degradation was dynamically monitored under an optical microscope following LIFU irradiation. As illustrated in Figure S5, the activation of SP@Lip-PEG under LIFU resulted in a gradual phase-transition phenomenon, transforming SP@Lip-PEG into microbubbles.

https://doi.org/10.1021/acsami.5c03394
ACS Appl. Mater. Interfaces 2025, 17, 29364−29378

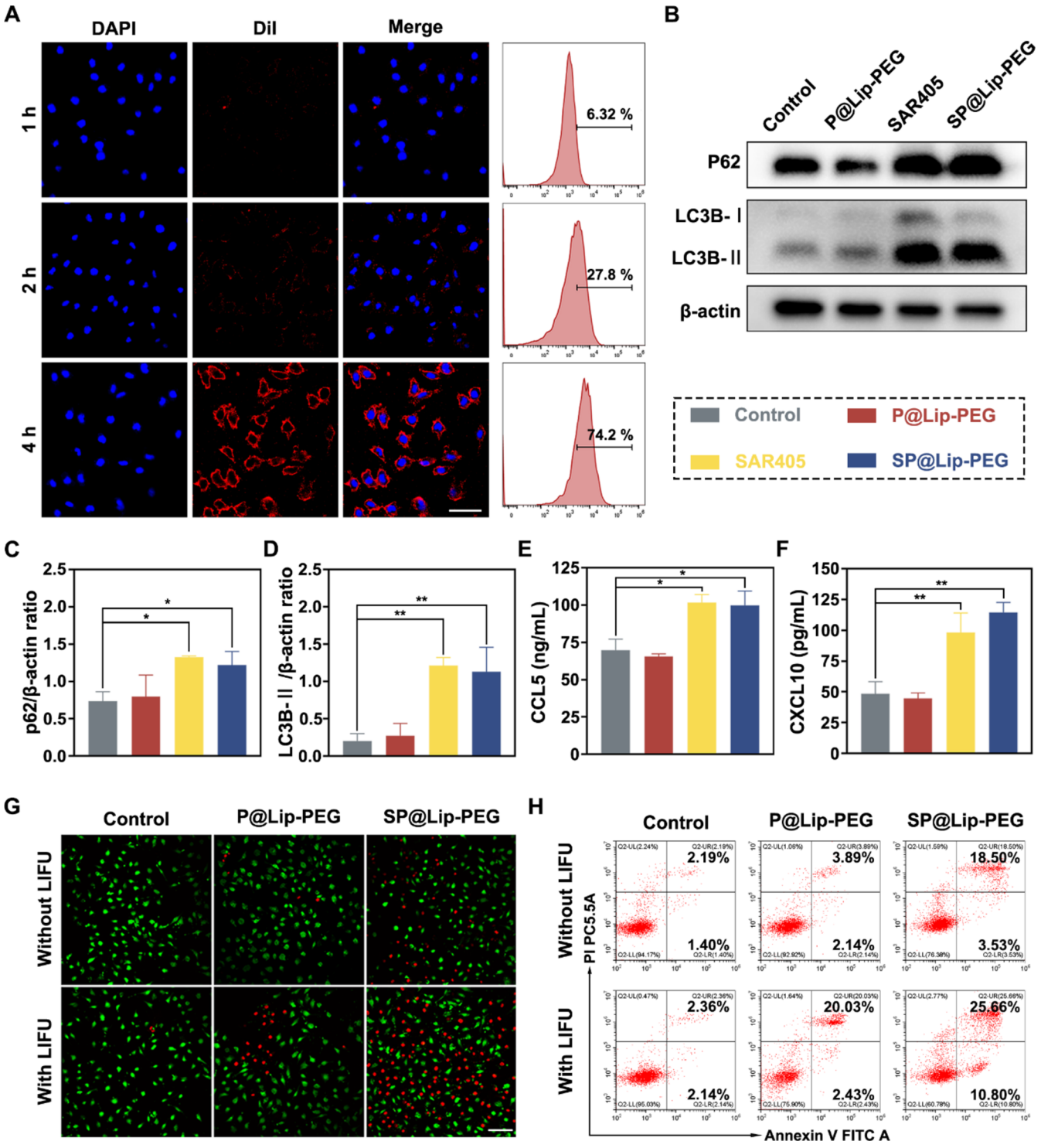

Figure 3. SP@Lip-PEG-mediated autophagy inhibition and antitumor proliferation. (A) CLSM and flow cytometric analysis of intracellular uptake behavior of DiI-labeled SP@Lip-PEG (Red fluorescence). Scale bar: 20 μm. (B) Western blot of β-actin, LC3B−I, LC3B−II, and p62 expression under different treatments. (C, D) The protein quantitative analysis was of p62/β-actin and LC3B−II/β-actin. (E, F) CCL5 and CXCL10 were secreted by B16−F10 cells after different treatments. (G) CLSM images of B16−F10 cells costained with calcein-AM/PI to discriminate between living (green fluorescence) and dead (red fluorescence) cells (Scale bar: 50 μm). (H) The apoptosis levels were measured by flow cytometry analysis after different treatments. Data are represented as mean ± SD (n = 3). *p < 0.05, **p < 0.01.

As the increase of exposure time, the microbubbles further inflated and collapsed. These results successfully demonstrated the phase-transition capability of SP@Lip-PEG, as well as its promising potential for realizing ultrasonic-responsive drug release.

To investigate the ultrasound-responsive drug release capability of SP@Lip-PEG, we employed a dialysis method to measure the cumulative release of SAR405 over 36 h (Figure 2A). With the absence of LIFU activation, less than 10% of SAR405 was released from SP@Lip-PEG during the

https://doi.org/10.1021/acsami.5c03394
ACS Appl. Mater. Interfaces 2025, 17, 29364−29378

first 6 h (Figure S6). However, after 6 h, SAR405 was released explosively owing to LIFU (3 W cm^{-2}, 3 min) excitation. After 24 h, the drug release tended to be flat. The 36-h cumulative release of SAR405 in the SP@Lip-PEG + LIFU group was about 61.85 ± 0.09%, significantly higher than the 34.14 ± 0.86% released in the SP@Lip-PEG group. According to the findings, SP@Lip-PEG demonstrated superior stability and minimal drug leakage, and the release of SAR405 can be accelerated under LIFU stimulation.

For personalized medicine, the real-time and adjustable release of drugs is essential. Afterward, we confirmed whether SP@Lip-PEG could perform as an on-demand drug release nanoplatform under multiple LIFU excitations. As shown in Figure 2B, LIFU stimulation was given every 4 h intervals in the first 12 h (4, 8, and 12 h). As expected, an explosive increase in the release rate of SAR405 was observed at the monitoring site (5, 9, and 13 h). After three cycles, the cumulative release rate of SAR405 reached 60.77 ± 4.13%, which was much higher than that of the control group (13.66 ± 0.82%). On the one hand, the ADV effects stimulated by ultrasound irradiation led to the phase change of SP@Lip-PEG into microbubbles, which activated the passive diffusion of encapsulated payloads to the outside microenvironment.[28] On the other hand, with repeated ultrasound excitations, numerous nanodroplets were converted into microbubbles, creating an obvious cavitation effect of ultrasound and promoting the considerable release of SAR405. Additionally, SAR405 release levels gradually recovered to initial levels without LIFU. This phenomenon was attributed to the fact that the stability of the remaining SP@Lip-PEG was unaffected without ultrasound excitation. In addition, image-guided drug release is essential for achieving precise delivery from drug carriers.[29] In the LIFU-responsive SP@Lip-PEG, the activation of LIFU successfully triggered the liquid−gas phase transition of PFP in the nanodroplet core, providing an ultrasonic visualization method to monitor drug release.

To quantitatively assess the ultrasound imaging capability of SP@Lip-PEG in response to LIFU, we evaluated the changes in imaging signals at various power levels applied to SP@Lip-PEG over different time points using a gel model. The ultrasound images clearly showed the real-time changes of SP@Lip-PEG under LIFU activation. As illustrated in Figure 2C, the ultrasound images in the control group exhibited no differences before and after LIFU irradiation. At 1 or 2 W cm^{-2}, the CEUS signal increased with both power and time, while the echo signal rose first and then fell at 3 or 4 W cm^{-2}. Taken together, these findings highlighted the excellent ultrasound imaging monitoring capability and the ultrasound-responsive drug release behavior of SP@Lip-PEG.

Encouraged by the impressive LIFU-response performance *in vitro*, we successfully confirmed that SP@Lip-PEG has the potential to enhance ultrasound imaging-guided drug release *in vivo*. First, a noninvasive FLI system was used to identify the optimal time point for the LIFU application. Following the tail vein injection of DiD-labeled SP@Lip-PEG in B16−F10 tumor-bearing C57BL/6 mice, significant accumulation was observed at 8 h, peaking around 24 h (Figure 2D,2E). Consequently, subsequent *in vivo* experiments were performed with LIFU excitation 8 h after nanodroplet injection. In the following step, the change of signal intensity in CEUS was utilized to validate the *in vivo* LIFU-response ability of SP@Lip-PEG in a tumor-bearing mouse model. There was almost no signal at the tumor site in mice prior to SP@Lip-PEG administration, and the signal was slightly increased after 8 h of injection, whereas the echogenic signal was enhanced dramatically after LIFU irradiation (Figure 2F,G). More importantly, we used UHPLC-MRM-MS/MS to directly quantify the drug content in the treated tumors. At 8 h, the intratumoral SAR405 concentration in the LIFU-stimulated group was approximately 3.3-fold higher than that in the control group (Figure 2H). These findings provide a rationale for achieving a controlled release of SAR405 during *in vivo* therapy. In summary, our delivery strategy not only addressed the limitations of the SAR405 application alone but also enabled the controlled release of SAR405 in a precise time and location through the UTD technique. This simple, safe, efficient, and image-guided approach presents hope for improving the therapeutic potential of SAR405.

3.3. Cellular Uptake Performance of SP@Lip-PEG *In Vitro*. To evaluate the cellular uptake of SP@Lip-PEG, DiI-labeled SP@Lip-PEG was fabricated. Then, the CLSM assay and flow cytometry assay were conducted. As shown in Figure 3A, after coincubating melanoma cells with SP@Lip-PEG for 1, 2, and 4 h, the distinct red fluorescence signals gradually formed around the cancer cells under CLSM observation. And the tendency of the results in flow cytometry was consistent with that in CLSM, suggesting the time-dependent internalization character of the DiI-labeled SP@Lip-PEG nanodroplet.

3.4. SP@Lip-PEG Prevents Autophagy and Induces CCL5 and CXCL10 *via* STAT1/IRF7. SAR405 is a Vps34-specific small-molecule autophagy inhibitor with anticancer activity.[30] We tracked the changes in autophagic flux in starved B16−F10 cells to investigate the impact of SAR405, including whether it could still influence autophagy levels after being loaded into nanodroplets. p62 can drive the ubiquitination-dependent autophagic degradation, which is a vital protein for assessing autophagic flux.[31] According to Western blot analysis, the SAR405 and SP@Lip-PEG + LIFU groups exhibited considerably higher p62 levels than the Control and P@Lip-PEG + LIFU groups (Figure 3B,3C). This indicated that SAR405 inhibited the autophagic flux. And the synthetic SP@Lip-PEG could produce the same effects when treated with LIFU. In addition, SAR405 can compromise vesicle transport from late endosomes to lysosomes, thus resulting in lysosome malfunction.[32] The autophagy-related protein LC3B−II highly accumulated in SAR405 and SP@Lip-PEG + LIFU groups, suggesting that the inhibition effect of SAR405 on autophagy could reduce LC3B−II lysosomal degradation (Figure 3B,D).

Besides, a recent study found that inhibiting autophagy with SAR405 can activate STAT1 and IRF7, causing tumor cells to release proinflammatory molecules CCL5 and CXCL10, which are essential for recruiting NK cells and $CD8^+$ T lymphocytes to the tumor site. As anticipated, we discovered that both SAR405 and SP@Lip-PEG upregulated the protein expression of STAT1 and IRF7 (Figures S7−S9). Subsequently, the cell supernatants after different treatments were collected, and the tumor cells in the SP@Lip-PEG + LIFU group secreted more CCL5 and CXCL10 than those in the P@Lip-PEG + LIFU group without drug loading (Figure 3E,F). In summary, SP@Lip-PEG can effectively inhibit the autophagy signaling pathway and significantly promote the production of chemokines CCL5 and CXCL10, contributing to the formation of an inflammatory tumor microenvironment.

3.5. Cytotoxicity Assay of SP@Lip-PEG *In Vitro*. Autophagy is beneficial for cells' resistance to harsh conditions, such as hunger, hypoxia, oxidative stress, and others.[33] In the

https://doi.org/10.1021/acsami.5c03394
ACS Appl. Mater. Interfaces 2025, 17, 29364−29378

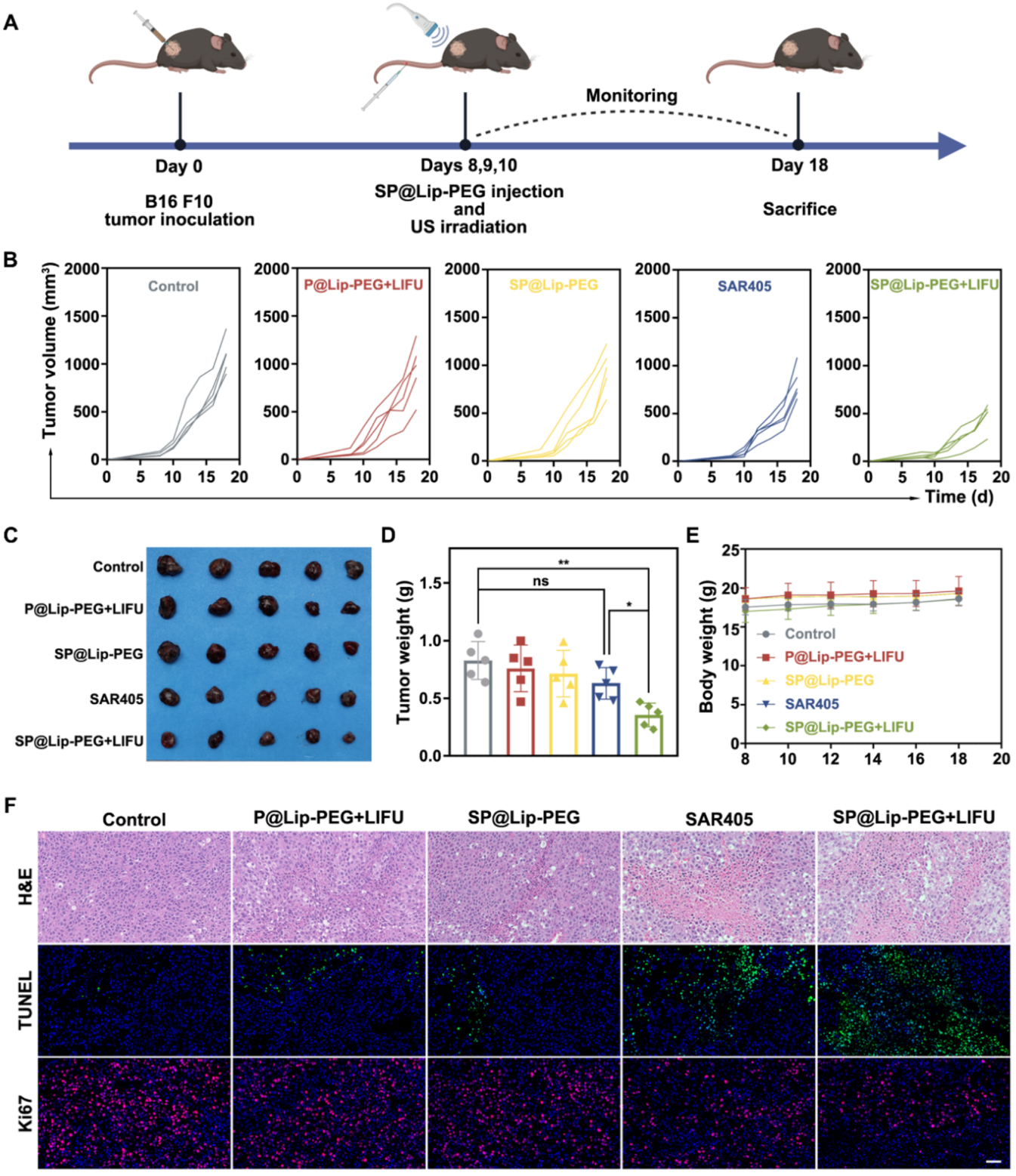

Figure 4. *In vivo* antitumor efficacy of SP@Lip-PEG + LIFU. (A) Schematic illustration of SP@Lip-PEG + LIFU treatment. Created with BioRender. (B) Individual tumor growth curves, (C) representative tumor images, and (D) tumor weights of the B16−F10 tumor-bearing mice after different treatments. (E) Body weight changes in each group. (F) H&E, TUNEL (green fluorescence), and Ki67 staining images (red fluorescence) of the B16−F10 tumors after various treatments. Scale bar: 50 μm. Data are presented as mean ± SD (n = 5), *p < 0.05, **p < 0.01.

hungry state, autophagy provides nutrition and material support for tumor cell survival by breaking down macromolecular substances, proteins, and organelles in the cell.[34] Accordingly, we assessed the effect of LIFU alone and SP@Lip-PEG in the combined regimen with LIFU on the B16−F10 cell viability. As illustrated in Figure S10, negligible toxicity to B16−F10 cells was observed across the tested LIFU power range (1, 2, 3, 4 W cm^{-2}, 3 min), indicating the good safety of LIFU. The cell viability decreased with the increase of SP@Lip-PEG concentration under LIFU irradiation (3 W cm^{-2}, 3

https://doi.org/10.1021/acsami.5c03394
ACS Appl. Mater. Interfaces 2025, 17, 29364−29378

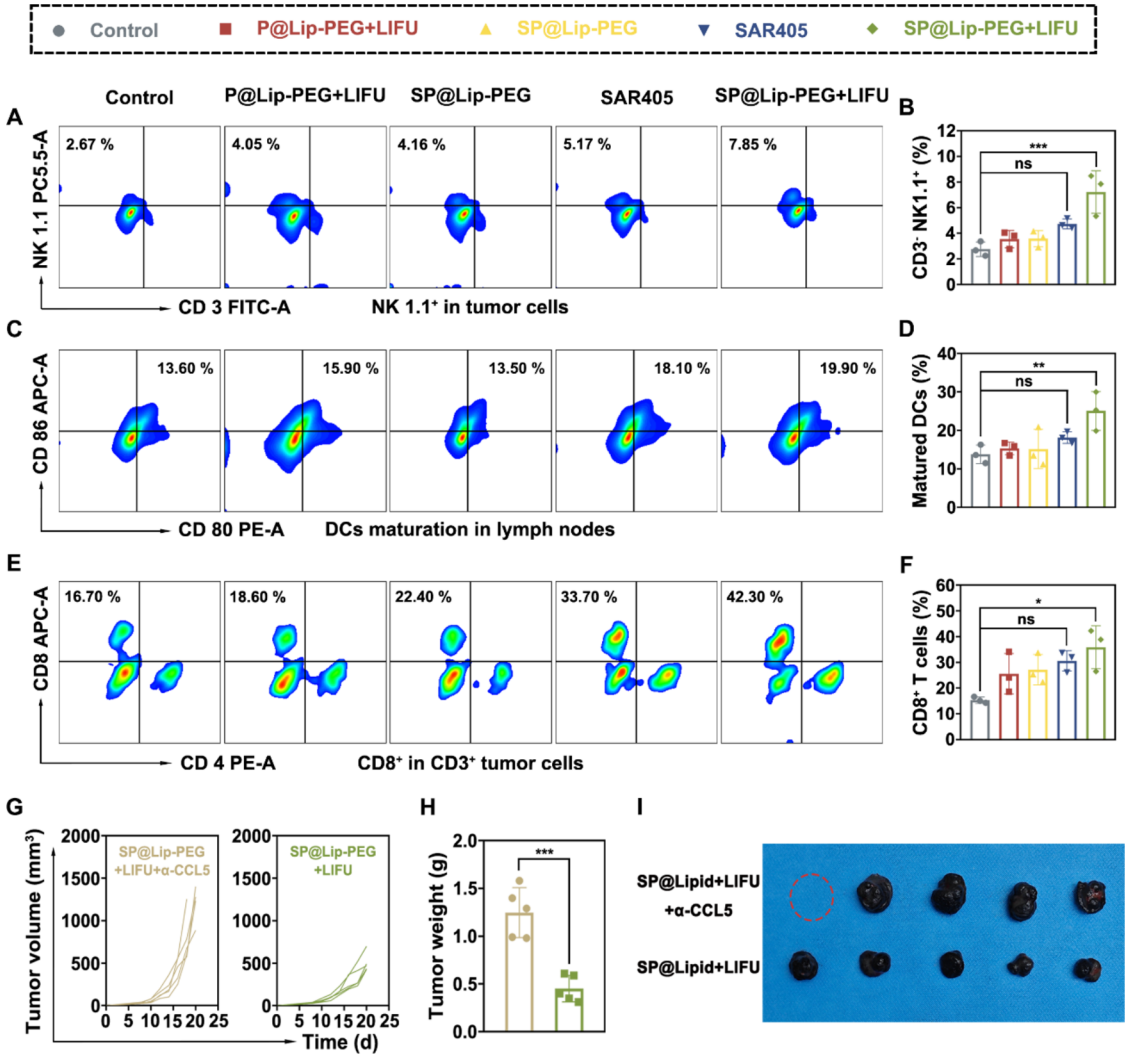

Figure 5. Immune landscape improvement of SP@Lip-PEG + LIFU treatment. (A) Flow cytometry plots of NK cells ($CD3^-$ $NK\text{-}1.1^+$) in the B16−F10 tumor site and the (B) corresponding quantification of NK cells (n = 3). (C) Flow cytometric analysis of matured DCs ($CD11c^+$ $CD80^+$ $CD86^+$) in draining lymph nodes of mice and (D) the corresponding quantitative analysis (n = 3). (E) Flow cytometry plots of CTLs ($CD3^+$ $CD8^+$) in the B16−F10 tumor site and the (F) corresponding quantification of CTLs (n = 3). (G) Individual tumor growth curves of the B16−F10 tumor-bearing mice after CCL5 blockade. (H) Tumor weights and (I) photographs of the B16−F10 tumors after treatments (n = 5). The red circle represented that the tumor burden reached the ethical end point ahead of schedule. All data are presented as the mean ± SD $^*p < 0.05$, $^{**}p < 0.01$, $^{***}p < 0.001$.

min) in cell proliferation assays (Figure S11). When the concentration of nanoparticles was 125 μg mL^{-1}, the inhibition plateaus about 50%, which provided a strong basis for further *in vitro* experiments. Next, the cell viability of the different treatment groups was compared. As depicted in Figure S12, a small amount of cell death occurred in the P@Lip-PEG + LIFU group, implying that the tumor cells may have been directly harmed by the cavitation effect caused by the explosion of phase-change P@Lip-PEG under ultrasound. The cell viability in the SP@Lip-PEG group was 72.18 ± 5.25%, possibly due to the passive release of SAR405 *via* the internalization of nanodroplets into the tumor cell, inhibiting autophagy in starved cancer cells. Remarkably, obvious toxicity was observed in the SP@Lip-PEG + LIFU group compared with other groups. On the one hand, the ultrasonic cavitation effect can directly damage tumor cells. On the other hand, the microjets generated by the ultrasonic cavitation effect can increase the permeability of the cell membrane and the internalization of nanoparticles. Under ultrasound, SAR405 was actively released from nanodroplets, significantly inhibiting tumor autophagy and weakening the resistance of the tumor cells to starvation. Moreover, CLSM images of calcein-AM/PI staining were used to detect dead and live cells after different treatments. There was a substantial increase in the red fluorescence signal of dead cells after the combination of SP@Lip-PEG with LIFU irradiation (Figure 3G). Correspondingly, flow cytometry revealed that the highest proportion of tumor cell apoptosis occurred in the SP@Lip-PEG + LIFU group (Figures 3H and S13). Collectively, these results illustrated that SP@Lip-PEG combined with LIFU treatment can overcome tumor proliferation by synergizing with ultrasound cavitation and autophagy inhibition.

3.6. Biocompatibility of SP@Lip-PEG *In Vivo*. For practical applications, it is essential to inspect the systemic toxicity characteristics of the nanoparticles. In advance of assessing the therapeutic efficacy of SP@Lip-PEG, the *in vivo* biosafety examination was performed *via* histopathology and hematology assay. Compared with the mice in the control

https://doi.org/10.1021/acsami.5c03394
ACS Appl. Mater. Interfaces 2025, 17, 29364−29378

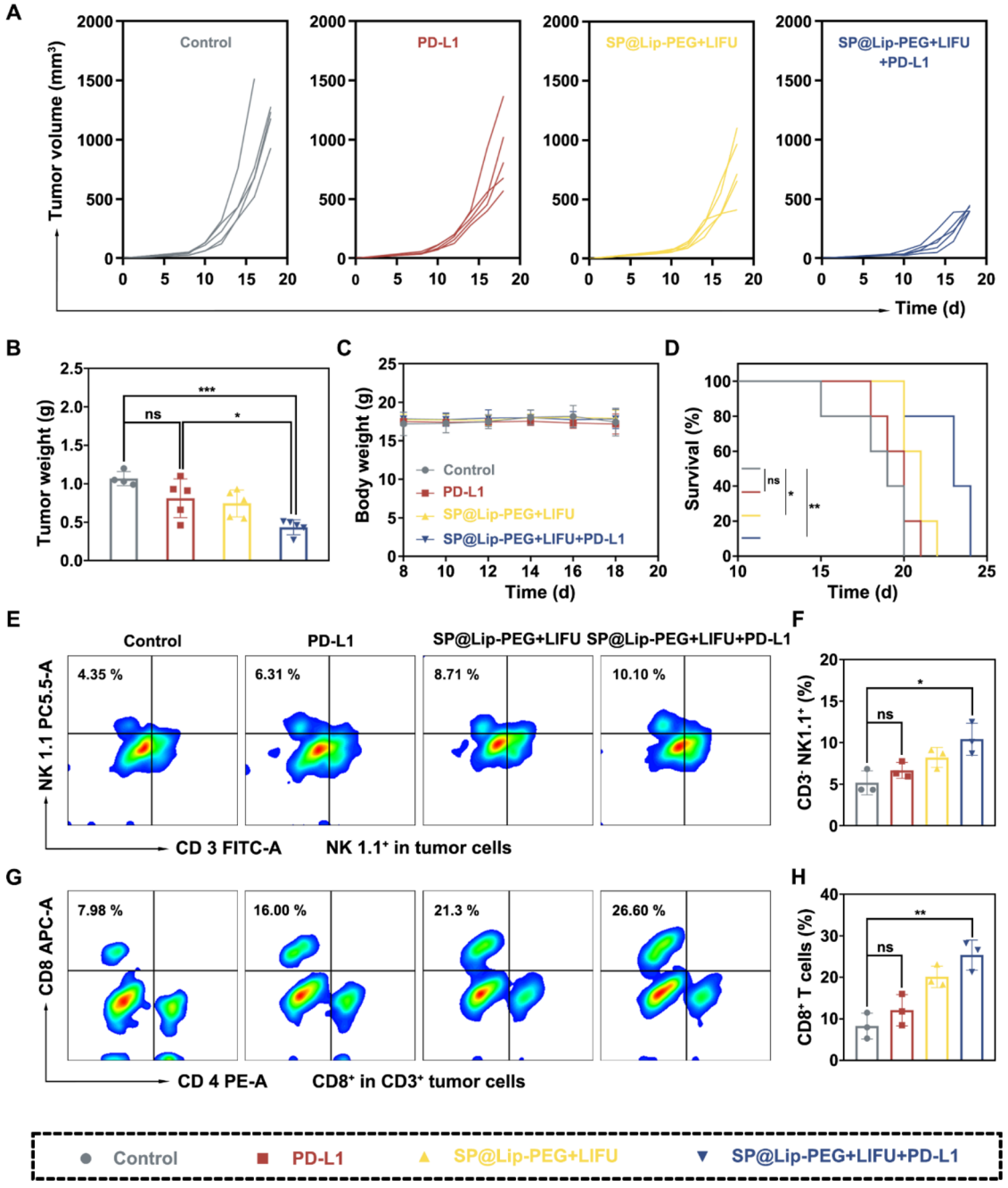

Figure 6. Improvement of anti-PD-L1 therapeutic efficacy in combination with SP@Lip-PEG + LIFU. (A) Individual tumor growth curves and (B) tumor weights of the B16−F10 tumors experienced different treatments (n = 5). (C) Body weight change in each group (n = 5). (D) Survival analysis of mice in different groups (n = 5). (E) Flow cytometry plots of NK cells in the B16−F10 tumor site and the (F) corresponding quantification of NK cells (n = 3). (G) Flow cytometry plots of CTLs in the B16−F10 tumor site and the (H) corresponding quantification of CTLs (n = 3). Data are presented as mean ± SD, *p < 0.05, **p < 0.01, ***p < 0.001.

group, those administrated with SP@Lip-PEG exhibited no apparent abnormalities in blood routine examination and serum biochemical indexes at different time points (Figure S14). In addition, H&E images of vital organs in each group also displayed no abnormal pathological changes over time (Figure S15). These above experimental findings validated that SP@Lip-PEG was biocompatible and could withstand further *in vivo* therapy.

3.7. Antitumor Efficacy *In Vivo*. Encouraged by the successful autophagy blockade effect of SP@Lip-PEG on facilitating the apoptosis of tumor cells and stimulating the release of proinflammatory factors *in vitro*, we further explored the ability of SP@Lip-PEG to inhibit tumor growth *in vivo*. The detailed procedure for evaluating the treatment efficacy of SP@Lip-PEG on B16−F10 melanoma-bearing mice is shown in Figure 4A. Tumor proliferation was tracked throughout the treatment. As depicted in Figure 4B−D, the tumors in the control group exhibited rapid growth, and treatment with SAR405 alone slowed the tumor growth rate. However, there was no significant statistical difference when compared to the control group. As anticipated, the SP@Lip-PEG + LIFU group exhibited an apparent reduction in tumor mass and growth

https://doi.org/10.1021/acsami.5c03394
ACS Appl. Mater. Interfaces 2025, 17, 29364−29378

proliferation speed. Notably, each mouse in the SAR405 group received a 40 μg injection of SAR405, and the injected SP@Lip-PEG only contained about 8.34 μg SAR405. Nonetheless, the significant difference in tumor weight between these two groups indeed underscored the therapeutic effectiveness of SP@Lip-PEG. The body weight of mice in the SP@Lip-PEG + LIFU group fluctuated negligibly during the observation period (Figure 4E). Based on the results, our nanodroplet delivery system, with no apparent toxic side effects, can considerably improve the pharmacokinetic metabolism of SAR405 and increase its accumulation in the tumor site to enhance its efficacy.

To further confirm the tumor-inhibiting effect, we performed a pathological analysis of the collected tumors by H&E, TUNEL, and Ki67 staining. In the SP@Lip-PEG + LIFU group, the H&E results demonstrated extensive necrosis in tumor tissue, accompanied by nuclear fragmentation, karyolysis, and karyopyknosis (Figure 4F). TUNEL staining in mice treated with SAR405 or SP@Lip-PEG + LIFU indicated a prevalence of green fluorescent signals in apoptotic cells and an attenuation of the proliferation-associated red fluorescent signals expressed by Ki67 staining. Overall, these results illustrated that SAR405 alone was not enough to induce effective tumor inhibition, while the ultrasound-stimulated nanovector could synergize with SAR405 to amplify the tumoricidal effect.

3.8. Improvement of Inflammatory Tumor Microenvironment *via* SP@Lip-PEG + LIFU. The TME, as the primary interaction site between tumor cells and the host immune system, plays a critical role in immunotherapy. The composition and infiltration of lymphocytes within the TME directly influence treatment efficacy. *In vitro*, the ability of SP@Lip-PEG to stimulate the production of CCL5 and CXCL10, which are critical in lymphocyte recruitment to the TME, has been confirmed.[35,36] Based on this, we used the melanoma model as a typical immune-cold tumor to evaluate the improvement of the immune microenvironment after the inhibition of autophagy by SP@Lip-PEG + LIFU.[37]

As shown in Figure 5A,B, there were noticeably more NK cells infiltrating the tumor site after the treatment of SP@Lip-PEG + LIFU when compared to the other four groups. NK cells could not only respond to control tumor burden in the early stages of the immune response but could also play important roles in promoting the recruitment of DCs and T cells into tumors.[38] As anticipated, the percentage of mature DCs in tumor-draining lymph nodes was considerably higher in the SP@Lip-PEG + LIFU group (25.07 ± 5.05%) than in the control group (13.80 ± 2.41%) (Figure 5C,5D). DCs, as one kind of immune cells with the strongest antigen-presenting ability, can present antigens to T cells after maturation, thus triggering the downstream adaptive immune response. In response to various stimuli, including chemokines, NK cells, and mature DC cells, SP@Lip-PEG + LIFU efficiently boosted the infiltration level of CTLs from 15.37 ± 1.22% (Control) to 35.90 ± 8.32% (SP@Lip-PEG + LIFU) (Figure 5E,F). The Western blot results demonstrated that the expression of LC3B−II increased in B16−F10 tumors after adding the autophagy inhibitor (Figures S16 and S17). Meanwhile, p62 was significantly upregulated in tumors treated with the SP@Lip-PEG + LIFU, confirming that the controlled release of SAR405 to strengthen the anti-autophagy strategy can be achieved *in vivo* through the LIFU-responsive phase-change nanodroplets delivery platform (Figures S16 and S18). Moreover, the results of Elisa showed that CXCL10 in TME had an upward trend, while CCL5 increased more significantly (Figures S19 and S20). Finally, to validate the function of CCL5, we blocked CCL5 in B16−F10 melanoma-bearing mice using CCL5 neutralizing antibodies. We found that the neutralization of CCL5 can significantly recover the tumor growth rate (Figure 5G). Moreover, the weight of the tumors and photographs after excision at the end of therapy corroborated the trend of tumor volume change (Figure 5H,5I). These results indicated that the migration of NK and T cells into the TME, driven by CCL5 and CXCL10, effectively transformed the cold TME status of the B16−F10 tumor into a hot TME status, thereby activating the immune response to inhibit tumor progression.

3.9. Synergistic Treatment of SP@Lip-PEG + LIFU and Anti-PD-L1. It is established that there is a positive correlation between the degree of CTL infiltration in the tumor and the effectiveness of anti-PD-L1 antibodies. Therefore, the remarkable effect of SP@Lip-PEG + LIFU on improving the infiltration of immune effector cells in the tumor microenvironment encouraged us to further explore whether autophagy inhibition therapy could cooperate with anti-PD-L1 immunotherapy. The combination treatment protocol for B16−F10 tumor-bearing mice is displayed in Figure S21. No apparent fluctuations in mice weight were found throughout the treatment, indicating that the procedure was harmless (Figure 6C). The tumor-suppressing effect of mice treated with anti-PD-L1 monotherapy was ineffective or served only in a few cases, which could be ascribed to the low responsiveness of B16−F10 to anti-PD-L1 antibodies and the obvious individual differences in the tumor microenvironment of mice (Figure 6A). Notably, tumor growth was markedly inhibited after being combined with SP@Lip-PEG + LIFU, indicating that the SAR405-induced inflammatory TME status strengthened the anti-PD-L1 immune response. In Figures S22 and 6B, both the typical images and weights of the resected tumors corroborated the preceding trend. In addition, the survival curve showed that anti-PD-L1 treatment did not significantly improve the survival time of mice compared to the control group. The SP@Lip-PEG + LIFU group achieved a certain survival benefit, but the survival time of mice in the combination treatment (SP@Lip-PEG + LIFU and anti-PD-L1) group was substantially longer than that in the other groups (Figure 6D).

Moreover, using flow cytometry technology, the abundance of NK cells and cytotoxic T cells in the tumor location was further inspected. The proportion of NK cells was 11.01 ± 1.91% in the SP@Lip-PEG + LIFU + PD-L1 group, which was approximately 2.01 and 1.56 times higher than those in the Control and PD-L1 groups, respectively (Figure 6E,F). Besides, the percentage of $CD8^+$ T cells in the combination group (25.37 ± 3.61%) was also significantly higher than that in the Control group (8.26 ± 3.10%) and the anti-PD-L1 monotherapy group (12.10 ± 3.76%) (Figure 6G,6H). In conclusion, SP@Lip-PEG + LIFU combined with the anti-PD-L1 antibody can mobilize the immune system of B16−F10 tumor-bearing mice and effectively improve the response rates to anti-PD-L1 therapy.

4. CONCLUSIONS

In summary, this study presented a meticulously engineered ultrasound-responsive phase-change nanodroplets nanoplatform to synergize autophagy blockade and ICB to generate a

https://doi.org/10.1021/acsami.5c03394
ACS Appl. Mater. Interfaces 2025, 17, 29364−29378

doomsday storm for melanoma. We demonstrated that the phase-change nanodroplets with LIFU activation exhibited an exceptional drug release performance and significantly inhibited the cellular autophagy pathways *via* the small-molecule agent SAR405. Crucially, *in vivo* experiments on murine models revealed that autophagy inhibition effectively fostered an inflammatory TME characterized by the increased infiltration of proinflammatory factors (CCL5 and CXCL10) and immune components (NK cells and $CD8^+$ T cells), along with facilitating the maturation status of DCs. Moreover, the cold melanoma TME was dexterously remodeled into hot status under the organic manipulation of inflammation and immune, significantly reinforcing the response efficiencies of anti-PD-L1 ICB therapy and leading to robust antitumor adaptive immune activation. Leveraging the clinical translational potential of nanodroplets alongside the noninvasive nature of ultrasound, this straightforward and potent drug delivery strategy offers a promising solution for addressing the current fatal limitations of ICB therapy.

■ ASSOCIATED CONTENT

Supporting Information

The Supporting Information is available free of charge at https://pubs.acs.org/doi/10.1021/acsami.5c03394.

Additional information as noted in the text, including the hydrodynamic size distribution of P@Lip-PEG and SP@Lip-PEG; encapsulation rate and drug-loading rate at different dosages; phase-transition images of SP@Lip-PEG; cumulative release curves; western blot images and quantitative analysis of STAT1 and IRF7 *in vitro*; cell viability of B16−F10; biosafety *in vivo*; western blot images and quantitative analysis of LC3B−II and p62*in vivo*; cytokine detection; schematic illustration of synergistic therapy; and digital photographs of removed tumors (PDF)

■ AUTHOR INFORMATION

Corresponding Authors

Chunyu Xia − *Department of Pharmacy, The Second Affiliated Hospital of Chongqing Medical University, Chongqing 400010, China*; Email: xiacy@hospital.cqmu.edu.cn

Pan Li − *Department of Ultrasound and Chongqing Key Laboratory of Ultrasound Molecular Imaging and Therapy, The Second Affiliated Hospital of Chongqing Medical University, Chongqing 400010, China*; orcid.org/0000-0002-0316-0355; Email: lipan@hospital.cqmu.edu.cn

Authors

Nianhong Wu − *Department of Ultrasound and Chongqing Key Laboratory of Ultrasound Molecular Imaging and Therapy, The Second Affiliated Hospital of Chongqing Medical University, Chongqing 400010, China*

Qin Zhang − *Department of Ultrasound and Chongqing Key Laboratory of Ultrasound Molecular Imaging and Therapy, The Second Affiliated Hospital of Chongqing Medical University, Chongqing 400010, China; Department of Radiology, Chongqing Traditional Chinese Medicine Hospital, Chongqing 400021, China; Chongqing College of Traditional Chinese Medicine, Chongqing 402760, China*

Rui Tang − *Department of Ultrasound and Chongqing Key Laboratory of Ultrasound Molecular Imaging and Therapy, The Second Affiliated Hospital of Chongqing Medical University, Chongqing 400010, China*

Liming Deng − *Department of Ultrasound, The First Affiliated Hospital of Chongqing Medical University, Chongqing 400016, China*

Yuting Cao − *Department of Ultrasound, The Second Xiangya Hospital, Central South University, Changsha, Hunan 410011, China*

Benxin Fu − *Department of Ultrasound, The Third Hospital of Mianyang, Sichuan Mental Health Center, Mianyang 621000, China*

Hongmei Dong − *Department of Ultrasound and Chongqing Key Laboratory of Ultrasound Molecular Imaging and Therapy, The Second Affiliated Hospital of Chongqing Medical University, Chongqing 400010, China*

Zeyan Huang − *Department of Ultrasound and Chongqing Key Laboratory of Ultrasound Molecular Imaging and Therapy, The Second Affiliated Hospital of Chongqing Medical University, Chongqing 400010, China*

Li Wan − *Department of Ultrasound and Chongqing Key Laboratory of Ultrasound Molecular Imaging and Therapy, The Second Affiliated Hospital of Chongqing Medical University, Chongqing 400010, China*

Hongye He − *Department of Ultrasound and Chongqing Key Laboratory of Ultrasound Molecular Imaging and Therapy, The Second Affiliated Hospital of Chongqing Medical University, Chongqing 400010, China*

Yi Lin − *Department of Ultrasound and Chongqing Key Laboratory of Ultrasound Molecular Imaging and Therapy, The Second Affiliated Hospital of Chongqing Medical University, Chongqing 400010, China*

Junjie Liu − *Department of Ultrasound and Chongqing Key Laboratory of Ultrasound Molecular Imaging and Therapy, The Second Affiliated Hospital of Chongqing Medical University, Chongqing 400010, China*

Complete contact information is available at: https://pubs.acs.org/10.1021/acsami.5c03394

Author Contributions

○N.W. and Q.Z.: contributed equally to this work. N.W.: Conceptualization, data curation, formal analysis, methodology, and writing—original manuscript. Q.Z.: Data curation, methodology, and funding acquisition. R.T.: Data curation and methodology validation. L.D.: Conducted some experiments and wrote—original manuscript. Y.C.: Writing—original manuscript. B.F.: Methodology validation. H.D. and Z.H.: Assisted in data curation. L.W., H.H., and Y.L.: Provided some experimental instructions. J.L.: Reviewed related data and figures. C.X.: Project administration, funding acquisition, reviewed, and wrote—review and editing. P.L.: Funding acquisition, project supervision, and writing—review and editing.

Notes

The authors declare no competing financial interest.

■ ACKNOWLEDGMENTS

This research was funded by the National Natural Science Foundation of China (82272025, 82404524), the Natural Science Foundation of Chongqing Municipality (cstc2021jcyj-msxmX0220), the Chongqing Graduate Student Research Innovation Project (CYB240201), and the Natural Science

Foundation of Chongqing, China (CSTB2024NSCQ-MSX0674).

■ ABBREVIATIONS

ICB,immune checkpoint blockade therapy; TME,tumor microenvironment; LIFU,low-intensity focused ultrasound; ADV,acoustic droplet vaporization; NK,natural killer; CTLs,cytotoxic T lymphocytes; UTD,ultrasound-targeted destruction; DPPC,1,2-Dipalmitoyl-*sn*-glycero-3-phosphocholine; DSPE-mPEG2000,1,2-distearoyl-*sn*-glycero-3-phosphoethanolamine-*N*-[methoxy(poly(ethylene glycol))-2000]; CLSM,confocal laser scanning microscopy; TEM,transmission electron microscopy; E.E.,encapsulation efficiency; CEUS,contrast-enhanced ultrasound; FLI,fluorescence imaging; TUNEL,terminal deoxynucleotidyl transferase dUTP nick end labeling; PDI,polydispersity index; FBS,fetal bovine serum

■ REFERENCES

(1) Korman, A. J.; Garrett-Thomson, S. C.; Lonberg, N. The foundations of immune checkpoint blockade and the ipilimumab approval decennial. *Nat. Rev. Drug Discovery* **2022**, *21* (7), 509−528.
(2) Lin, X.; Kang, K.; Chen, P.; Zeng, Z.; Li, G.; Xiong, W.; Yi, M.; Xiang, B. Regulatory mechanisms of PD-1/PD-L1 in cancers. *Mol. Cancer* **2024**, *23* (1), No. 108.
(3) Ribas, A.; Hamid, O.; Daud, A.; Hodi, F. S.; Wolchok, J. D.; Kefford, R.; Joshua, A. M.; Patnaik, A.; Hwu, W.-J.; Weber, J. S.; Gangadhar, T. C.; Hersey, P.; Dronca, R.; Joseph, R. W.; Zarour, H.; Chmielowski, B.; Lawrence, D. P.; Algazi, A.; Rizvi, N. A.; Hoffner, B.; Mateus, C.; Gergich, K.; Lindia, J. A.; Giannotti, M.; Li, X. N.; Ebbinghaus, S.; Kang, S. P.; Robert, C. Association of Pembrolizumab With Tumor Response and Survival Among Patients With Advanced Melanoma. *JAMA* **2016**, *315* (15), 1600−1609.
(4) Khosravi, G. R.; Mostafavi, S.; Bastan, S.; Ebrahimi, N.; Gharibvand, R. S.; Eskandari, N. Immunologic tumor microenvironment modulators for turning cold tumors hot. *Cancer Commun.* **2024**, *44* (5), 521−553.
(5) Galon, J.; Bruni, D. Approaches to treat immune hot, altered and cold tumours with combination immunotherapies. *Nat. Rev. Drug Discovery* **2019**, *18* (3), 197−218.
(6) Wu, B.; Zhang, B.; Li, B.; Wu, H.; Jiang, M. Cold and hot tumors: from molecular mechanisms to targeted therapy. *Signal Transduction Targeted Ther.* **2024**, *9* (1), No. 274.
(7) Huang, J.; Xiao, Z.; An, Y.; Han, S.; Wu, W.; Wang, Y.; Guo, Y.; Shuai, X. Nanodrug with dual-sensitivity to tumor microenvironment for immuno-sonodynamic anti-cancer therapy. *Biomaterials* **2021**, *269*, No. 120636.
(8) Oladejo, M.; Paulishak, W.; Wood, L. Synergistic potential of immune checkpoint inhibitors and therapeutic cancer vaccines. *Semin. Cancer Biol.* **2023**, *88*, 81−95.
(9) Yi, Y.; Yu, M.; Li, W.; Zhu, D.; Mei, L.; Ou, M. Vaccine-like nanomedicine for cancer immunotherapy. *J. Controlled Release* **2023**, *355*, 760−778.
(10) Zheng, J.; Mo, J.; Zhu, T.; Zhuo, W.; Yi, Y.; Hu, S.; Yin, J.; Zhang, W.; Zhou, H.; Liu, Z. Comprehensive elaboration of the cGAS-STING signaling axis in cancer development and immunotherapy. *Mol. Cancer* **2020**, *19* (1), No. 133.
(11) Ahn, J.; Xia, T.; Konno, H.; Konno, K.; Ruiz, P.; Barber, G. N. Inflammation-driven carcinogenesis is mediated through STING. *Nat. Commun.* **2014**, *5* (1), No. 5166.
(12) Wang, L.; You, H. M.; Meng, H. W.; Pan, X. Y.; Chen, X.; Bi, Y. H.; Zhang, Y. F.; Li, J. J.; Yin, N. N.; Zhang, Z. W.; Huang, C.; Li, J. STING-mediated inflammation contributes to Gao binge ethanol feeding model. *J. Cell. Physiol.* **2022**, *237* (2), 1471−1485.
(13) Noman, M. Z.; Parpal, S.; Van Moer, K.; Xiao, M.; Yu, Y.; Arakelian, T.; Viklund, J.; De Milito, A.; Hasmim, M.; Andersson, M.; Amaravadi, R. K.; Martinsson, J.; Berchem, G.; Janji, B. Inhibition of Vps34 reprograms cold into hot inflamed tumors and improves anti-PD-1/PD-L1 immunotherapy (vol 6, eaax7881, 2020). *Sci. Adv.* **2021**, *7* (15), No. eaax7881.
(14) Deretic, V. Autophagy in inflammation, infection, and immunometabolism. *Immunity* **2021**, *54* (3), 437−453.
(15) Wang, Y.; Lei, H.; Yan, B.; Zhang, S.; Xu, B.; Lin, M.; Shuai, X.; Huang, J.; Pang, J. Tumor acidity-activatable macromolecule autophagy inhibitor and immune checkpoint blockade for robust treatment of prostate cancer. *Acta Biomater.* **2023**, *168*, 593−605.
(16) Yamamoto, K.; Venida, A.; Yano, J.; Biancur, D. E.; Kakiuchi, M.; Gupta, S.; Sohn, A. S. W.; Mukhopadhyay, S.; Lin, E. Y.; Parker, S. J.; Banh, R. S.; Paulo, J. A.; Wen, K. W.; Debnath, J.; Kim, G. E.; Mancias, J. D.; Fearon, D. T.; Perera, R. M.; Kimmelman, A. C. Autophagy promotes immune evasion of pancreatic cancer by degrading MHC-I. *Nature* **2020**, *581* (7806), 100−105.
(17) Yu, Y.; Bogdan, M.; Noman, M. Z.; Parpal, S.; Bartolini, E.; Van Moer, K.; Kleinendorst, S. C.; Bilgrav Saether, K.; Trésaugues, L.; Silvander, C.; Lindström, J.; Simeon, J.; Timson, M. J.; Al-Hashimi, H.; Smith, B. D.; Flynn, D. L.; Alexeyenko, A.; Viklund, J.; Andersson, M.; Martinsson, J.; Pokrovskaja Tamm, K.; De Milito, A.; Janji, B. Combining VPS34 inhibitors with STING agonists enhances type I interferon signaling and anti-tumor efficacy. *Mol. Oncol.* **2024**, *18* (8), 1904−1922.
(18) Alamassi, M. N.; Chia, S. L.; Abdullah, C. A. C.; Masarudin, M. J. Increased efficacy of biologics following inhibition of autophagy in A549 lung cancer cells in bimodal treatment of doxorubicin and SAR405-loaded chitosan nanoparticles. *OpenNano* **2023**, *11*, No. 100142.
(19) Tang, L.; Zhang, H.; Zhou, F.; Wei, Q.; Du, M.; Wu, J.; Li, C.; Luo, W.; Zhou, J.; Wang, X.; Chen, Z.; Zhang, Y.; Huang, Z.; Wu, Z.; Wen, Y.; Jiang, H.; Liao, D.; Kou, H.; Xiong, W.; Mei, H.; Hu, Y. Targeting autophagy overcomes cancer-intrinsic resistance to CAR-T immunotherapy in B-cell malignancies. *Cancer Commun.* **2024**, *44* (3), 408−432.
(20) Li, K.; Chen, H.-S.; Li, D.; Li, H.-H.; Wang, J.; Jia, L.; Wu, P.-F.; Long, L.-H.; Hu, Z.-L.; Chen, J.-G.; Wang, F. SAR405, a Highly Specific VPS34 Inhibitor, Disrupts Auditory Fear Memory Consolidation of Mice via Facilitation of Inhibitory Neurotransmission in Basolateral Amygdala. *Biol. Psychiatry* **2019**, *85* (3), 214−225.
(21) Li, B.; Zhong, H.; Wei, H.; Chen, G.; Lin, M.; Huang, S.; Zhang, Q.; Xing, C.; Li, T.; Huang, J.; Shuai, X. Ultrasound-irradiated bindable microbomb opens the blood-brain barrier to enhance glioma therapy. *Nano Today* **2024**, *56*, No. 102312.
(22) Li, B.; Chen, G.; Zhong, H.; Li, T.; Lin, M.; Wei, H.; Zhang, Q.; Chen, Q.; Huang, J.; Shuai, X. γ-Glutamyl transpeptidase-activable nanoprobe crosses the blood-brain barrier for immuno-sonodynamic therapy of glioma. *Nat. Commun.* **2024**, *15* (1), No. 10418.
(23) Shakya, G.; Cattaneo, M.; Guerriero, G.; Prasanna, A.; Fiorini, S.; Supponen, O. Ultrasound-responsive microbubbles and nanodroplets: A pathway to targeted drug delivery. *Adv. Drug Delivery Rev.* **2024**, *206*, No. 115178.
(24) Wang, X.; Li, C.; Wang, Y.; Chen, H.; Zhang, X.; Luo, C.; Zhou, W.; Li, L.; Teng, L.; Yu, H.; Wang, J. Smart drug delivery systems for precise cancer therapy. *Acta Pharm. Sin. B* **2022**, *12* (11), 4098−4121.
(25) Huang, J.; Zhang, L.; Zheng, J.; Lin, Y.; Leng, X.; Wang, C.; Li, P.; Feng, L. Microbubbles-assisted ultrasonication to promote tumor accumulation of therapeutics and modulation of tumor microenvironment for enhanced cancer treatments. *Biomaterials* **2023**, *299*, No. 122181.
(26) Chen, Q.; Huang, J. B.; Ye, Y. L.; Hu, A. Z.; Xu, B. X.; Hu, D.; Wang, L. L.; Xing, L. J.; Chen, S. T.; Gui, X. A.; Tong, W. Z.; Gan, Y. M.; Zheng, T. T.; Zheng, J.; Liu, L.; Hu, G. X. Delivery of hydroxycamptothecin via sonoporation: An effective therapy for liver fibrosis. *J. Controlled Release* **2023**, *358*, 319−332.
(27) Liu, S. B.; Zhang, Y.; Liu, Y.; Wang, W. K.; Gao, S. C.; Yuan, W. T.; Sun, Z. Q.; Liu, L.; Wang, C. Z. Ultrasound-targeted microbubble destruction remodels tumour microenvironment to improve immunotherapeutic effect. *Br. J. Cancer* **2023**, *128* (5), 715−725.

https://doi.org/10.1021/acsami.5c03394
ACS Appl. Mater. Interfaces 2025, 17, 29364−29378

(28) Hou, J.; Zhou, J.; Chang, M.; Bao, G.; Xu, J.; Ye, M.; Zhong, Y.; Liu, S.; Wang, J.; Zhang, W.; Ran, H.; Wang, Z.; Chen, Y.; Guo, D. LIFU-responsive nanomedicine enables acoustic droplet vaporization-induced apoptosis of macrophages for stabilizing vulnerable atherosclerotic plaques. *Bioact. Mater.* **2022**, *16*, 120−133.
(29) Priester, M. I.; ten Hagen, T. L. M. Image-guided drug delivery in nanosystem-based cancer therapies. *Adv. Drug Delivery Rev.* **2023**, *192*, No. 114621.
(30) Pasquier, B. SAR405, a PIK3C3/Vps34 inhibitor that prevents autophagy and synergizes with MTOR inhibition in tumor cells. *Autophagy* **2015**, *11* (4), 725−726.
(31) Vargas, J. N. S.; Hamasaki, M.; Kawabata, T.; Youle, R. J.; Yoshimori, T. The mechanisms and roles of selective autophagy in mammals. *Nat. Rev. Mol. Cell Biol.* **2023**, *24* (3), 167−185.
(32) Zhou, P.; Li, Y.; Li, B.; Zhang, M.; Xu, C.; Liu, F.; Bian, L.; Liu, Y.; Yao, Y.; Li, D. Autophagy inhibition enhances celecoxib-induced apoptosis in osteosarcoma. *Cell Cycle* **2018**, *17* (8), 997−1006.
(33) Kocaturk, N. M.; Akkoc, Y.; Kig, C.; Bayraktar, O.; Gozuacik, D.; Kutlu, O. Autophagy as a molecular target for cancer treatment. *Eur. J. Pharm. Sci.* **2019**, *134*, 116−137.
(34) Kitada, M.; Koya, D. Autophagy in metabolic disease and ageing. *Nat. Rev. Endocrinol.* **2021**, *17* (11), 647−661.
(35) Nagarsheth, N.; Wicha, M. S.; Zou, W. Chemokines in the cancer microenvironment and their relevance in cancer immunotherapy. *Nat. Rev. Immunol.* **2017**, *17* (9), 559−572.
(36) Schmidt, L.; Eskiocak, B.; Kohn, R.; Dang, C.; Joshi, N. S.; DuPage, M.; Lee, D.-Y.; Jacks, T. Enhanced adaptive immune responses in lung adenocarcinoma through natural killer cell stimulation. *Proc. Natl. Acad. Sci. U.S.A.* **2019**, *116* (35), 17460−17469.
(37) Shi, W.; Liu, N.; Liu, Z.; Yang, Y.; Zeng, Q.; Wang, Y.; Song, L.; Hu, F.; Fu, J.; Chen, J.; Wu, M.; Zhou, L.; Zhu, F.; Gong, L.; Zhu, J.; Jiang, L.; Lu, H. Next-generation anti-PD-L1/IL-15 immunocytokine elicits superior antitumor immunity in cold tumors with minimal toxicity. *Cell Rep. Med.* **2024**, *5* (5), No. 101531.
(38) Kyrysyuk, O.; Wucherpfennig, K. W. Designing Cancer Immunotherapies That Engage T Cells and NK Cells. *Annu. Rev. Immunol.* **2023**, *41* (1), 17−38.

https://doi.org/10.1021/acsami.5c03394
ACS Appl. Mater. Interfaces 2025, 17, 29364−29378